DESY 05-079

Is it possible to tell the difference between fermionic and bosonic hot dark matter?

Steen Hannestad

Department of Physics and Astronomy
University of Aarhus, DK-8000 Aarhus C, Denmark

Andreas Ringwald

Deutsches Elektronen-Synchrotron DESY, Hamburg, Germany

Huitzu Tu

Department of Physics and Astronomy
University of Aarhus, DK-8000 Aarhus C, Denmark

Yvonne Y. Y. Wong

Deutsches Elektronen-Synchrotron DESY, Hamburg, Germany

E-mail: sth@phys.au.dk, andreas.ringwald@desy.de, huitzu@phys.au.dk, yvonne.wong@desy.de

Abstract. We study the difference between thermally produced fermionic and bosonic hot dark matter in detail. In the linear regime of structure formation, their distinct free-streaming behaviours can lead to pronounced differences in the matter power spectrum. While not detectable with current cosmological data, such differences will be clearly observable with upcoming large scale weak lensing surveys for particles as light as $m_{\rm HDM} \sim 0.2$ eV. In the nonlinear regime, bosonic hot dark matter is not subject to the same phase space constraints that severely limit the amount of fermionic hot dark matter infall into cold dark matter halos. Consequently, the overdensities in fermionic and bosonic hot dark matter of equal particle mass can differ by more than a factor of five in the central part of a halo. However, this unique manifestation of quantum statistics may prove very difficult to detect unless the mass of the hot dark matter particle and its decoupling temperature fall within a very narrow window, $1 \lesssim m_{\rm HDM}/{\rm eV} \lesssim 4$ and $g_* \lesssim 30$. In this case, hot dark matter infall may have some observable consequences for the nonlinear power spectrum and hence the weak lensing convergence power spectrum at $\ell \sim 10^3 \to 10^4$ at the percent level.

1. Introduction

With the advent of precision measurements of the cosmic microwave background (CMB), large scale structure (LSS) of galaxies, and distant type Ia supernovae, a new paradigm of cosmology has been established. In this new standard model, the geometry is flat so that $\Omega_{\rm total} = 1$, and the total energy density is made up of matter ($\Omega_m \sim 0.3$) [comprising of baryons ($\Omega_b \sim 0.05$) and cold dark matter ($\Omega_{\rm CDM} \sim 0.25$)], and dark energy ($\Omega_X \sim 0.7$). With only a few free parameters this model provides an excellent fit to all current observations [1, 2, 3, 4]. In turn, this allows for constraints on other, nonstandard cosmological parameters. One very interesting possibility discussed widely in the literature is a subdominant contribution to the total energy density in the form of neutrino hot dark matter (HDM) and hence limits on the neutrino mass.

In general, any fermionic dark matter species ψ which decouples while relativistic obeys the relation

$$\Omega_\psi h^2 = g \times \frac{10.75}{g_{*,\psi}} \times \frac{m_\psi}{183\,\mathrm{eV}}, \tag{1.1}$$

where m_ψ is the ψ particle's mass, g its number of internal degrees of freedom, and $g_{*,\psi}$ the effective number of degrees of freedom in the plasma at the time of ψ decoupling. By entropy conservation, $g_{*,\psi}$ can be related to the effective temperature of the species via $g_{*,\psi} T_\psi^3 = g_{*,\nu} T_\nu^3$, with the subscript ν referring to the standard model neutrinos. Standard model neutrinos decouple in the early universe at a temperature of order $2 \to 3$ MeV, when $g_* = 10.75$. Thus, just from demanding $\Omega_\nu \lesssim \Omega_{\rm total} \simeq 1$, one finds the well known upper limit on the neutrino mass [5, 6], $m_\nu \lesssim 46/N_\nu$ eV, assuming N_ν neutrino flavours with degenerate masses.

However, a much stronger limit on the neutrino mass can be derived by noticing that the thermal history of HDM is very different from that of CDM. By definition HDM becomes nonrelativistic only at very late times. At early times free-streaming of the HDM particles causes essentially all of their own perturbations to be erased on scales below the free-streaming length [7],

$$\lambda_{\rm FS} \sim \frac{20\ \mathrm{Mpc}}{\Omega_\psi h^2} \left(\frac{T_\psi}{T_\nu}\right)^4 \left[1 + \log\left(3.9 \frac{\Omega_\psi h^2}{\Omega_m h^2} \left(\frac{T_\nu}{T_\psi}\right)^2\right)\right], \tag{1.2}$$

leaving only perturbations in the nonrelativistic matter (CDM and baryons). On scales larger than $\lambda_{\rm FS}$, however, HDM behaves like CDM. Thus, the net result is a suppression of the overall level of fluctuations on scales below $\lambda_{\rm FS}$.

In terms of the present matter power spectrum, $P(k,\tau) \equiv |\delta|^2(k,\tau)$, where $\delta(k,\tau)$ is the Fourier transform of the density perturbations $\delta(x,\tau)$, early free-streaming leads to a suppression of power at $k \gg 2\pi/\lambda_{\rm FS}$ by roughly

$$\frac{\Delta P(k,\tau)}{P(k,\tau)} \simeq -8 \times \frac{\Omega_\psi}{\Omega_m}, \tag{1.3}$$

where the factor eight is derived from a numerical solution of the Boltzmann equation [9]. Equation (1.3) applies only when $\Omega_\psi \ll \Omega_m$; when Ω_ψ dominates, the spectrum

suppression becomes exponential as in the pure HDM model. Note that the free-streaming scale becomes very small for very large values of $g_* \ (\sim 10^3)$. In this case, the species should be better known as warm dark matter (see [8] for a recent discussion of mass bounds on warm dark matter).

Of course, a suppression of small scale power in the present day matter power spectrum could have its roots in a number of other factors, such as a lower matter density, a higher relativistic energy density, a primordial power spectrum with broken scale invariance, etc.. Therefore, in order to constrain the HDM energy density and hence the mass of the HDM particle, it is necessary to combine LSS with CMB measurements. Currently available cosmological data constrain the sum of light, standard model neutrino masses to $\sum m_\nu \simeq 0.5 \rightarrow 2$ eV, depending both on the data sets used and on assumptions about other cosmological parameters [3, 10, 11, 12, 13, 14, 15, 16, 17].

While cosmological limits on HDM have mainly been discussed for neutrinos, they apply equally well to bosons and thermal relics with $g_* > 10.75$ [18]. Many such hypothetical HDM candidates exist, including the likes of axions [19, 20], majorons, gravitinos [21], axinos [22], etc.. An even more exotic scenario recently discussed in the literature is the possibility that neutrinos violate Fermi–Dirac spin statistics and behave like bosons [23, 24]. It is clearly worthwhile to study the differences between these various HDM species arising from their quantum statistics. As we shall see later, there are fundamental differences in their clustering properties which might be observable with future, high precision probes.

Indeed, the purpose of this paper is to study the differences between fermionic and bosonic HDM. From here on we consider two generic HDM species: A single massive Majorana fermion ψ with $g = 2$, and a single massive scalar ϕ with $g = 1$. Unless otherwise indicated, we shall assume, throughout the present work, a cosmological constant Λ, three massless standard model neutrinos, and the following cosmological parameters: $\{\Omega_m, \Omega_\Lambda, \Omega_b, h, \sigma_8\} = \{0.3, 0.7, 0.05, 0.7, 0.9\}$.

The paper is structured as follows. In the next section we discuss structure formation in the linear regime. Section 3 deals with nonlinear structure formation, including hot dark matter infall into CDM halos. We consider gravitational lensing as a probe of structure formation in section 4, and section 5 contains our conclusions.

2. Structure formation in the linear regime

A thermal relic that decouples from the cosmic plasma while relativistic assumes either the relativistic Fermi–Dirac (FD, "+") or Bose–Einstein (BE, "−") distribution,

$$f(p) = \frac{1}{\exp(p/T) \pm 1}. \tag{2.1}$$

If the particle is stable and no heavier particle decays into it, its phase space distribution is preserved with the expansion of the universe. Today, a single massive $g = 2$ Majorana fermion ψ and a $g = 1$ scalar ϕ are expected to contribute to the total energy density

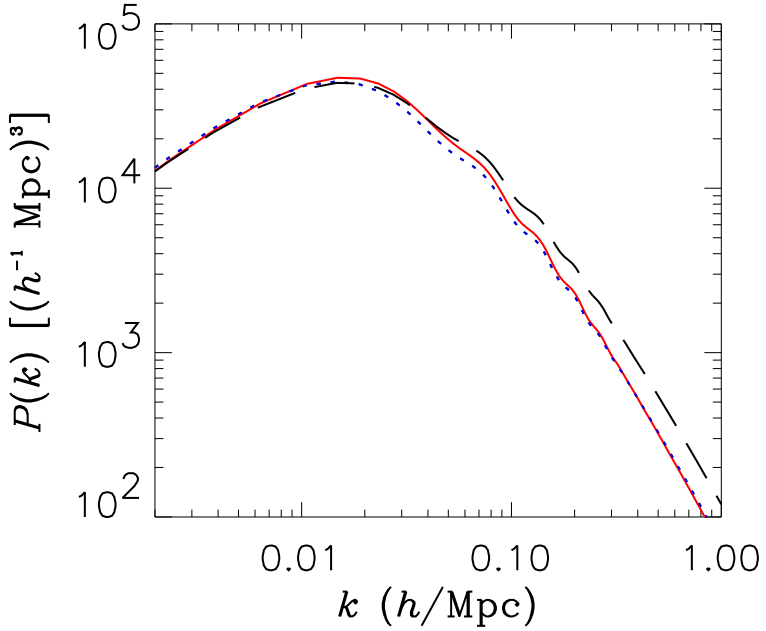

Figure 1. Linear power spectra for two different ΛHCDM models. The blue (dotted) line shows a model with three massless neutrinos and one massive Majorana fermion, contributing $\Omega_\psi = 0.02$. The red (solid) line shows the same, but with a massive scalar instead. The black (dashed) line is the standard ΛCDM model with no HDM. Note that these spectra have been normalised to have the same amplitude on large scales.

at fractions of

$$\Omega_\psi h^2 = 2 \times \frac{10.75}{g_{*,\psi}} \times \frac{m_\psi}{183\,\mathrm{eV}}, \tag{2.2}$$

$$\Omega_\phi h^2 = \frac{4}{3} \times 1 \times \frac{10.75}{g_{*,\phi}} \times \frac{m_\phi}{183\,\mathrm{eV}}. \tag{2.3}$$

Already, we can see that for any given Ω_{HDM}, the mass of the scalar is necessarily a factor 3/2 higher than that of the fermion.

With regard to structure formation, the amount of suppression in the matter power spectrum due to HDM is essentially dependent only on the ratio $\Omega_{\mathrm{HDM}}/\Omega_m$, i.e., it depends only on the lack of dark matter. Therefore, on both very small and very large scales, fermion and scalar models with identical Ω_{HDM} are virtually indistinguishable to the naked eye. However, for scales close to the free-streaming length (and therefore also to the scale of matter–radiation equality for sub-eV hot dark matter), there is a pronounced difference. The reason is that for the same Ω_{HDM}, the more massive scalar particle exhibits less free-streaming. This in turn allows for an increased fluctuation amplitude around the free-streaming scale. In Figure 1 we show the power spectra for two models with identical $\Omega_{\mathrm{HDM}} = 0.02$ and $g_* = 10.75$ (corresponding to $m_\psi = 0.9$ eV for the fermion model and $m_\phi = 1.3$ eV for the scalar model). As can be seen, the scalar model has more power at $k \sim 0.01 \rightarrow 0.1\ h$ Mpc. For comparison we also show the standard ΛCDM model, which has the same parameters, except that $\Omega_{\mathrm{HDM}} = 0$.

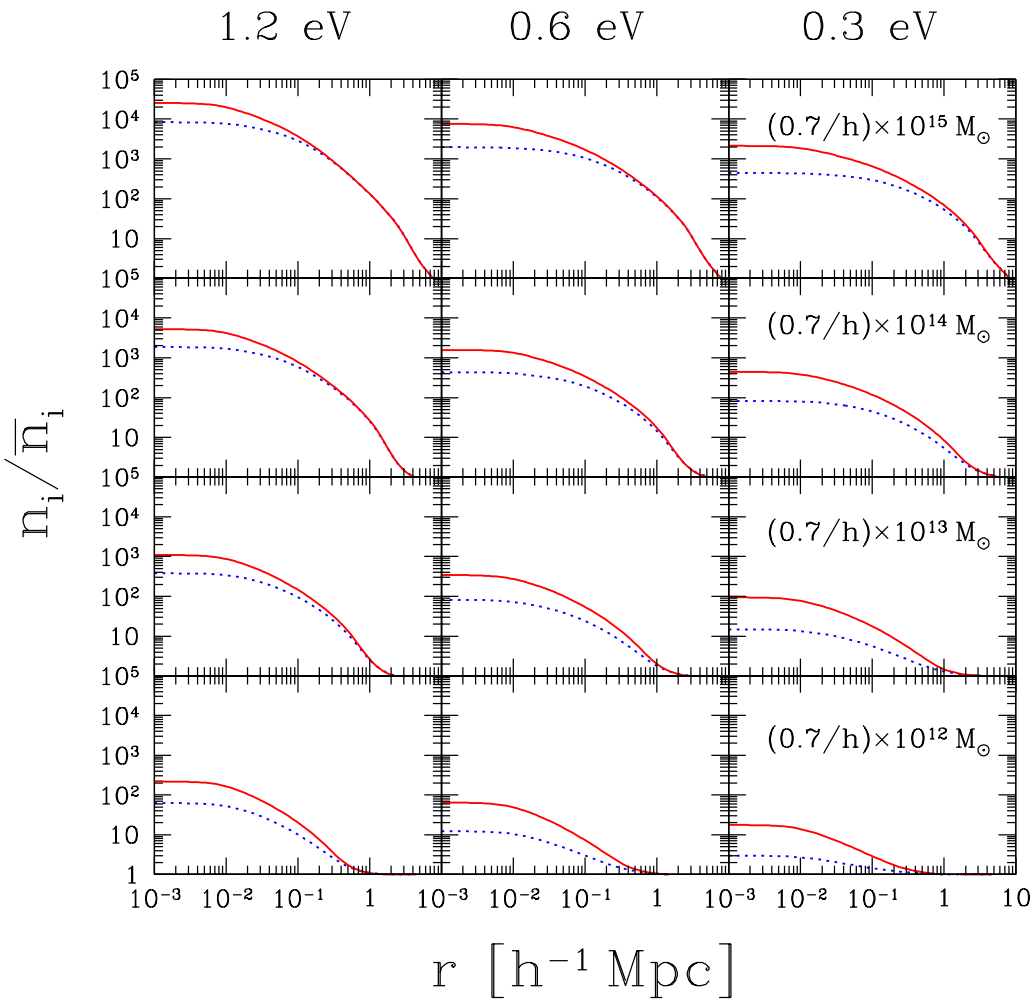

Figure 2. Number densities of HDM expected for $g_* = 10.75$ and the indicated halo and HDM masses at $z = 0$, normalised to the cosmological average $\bar{n}_i$. Red (solid) lines represent bosons, while blue (dotted) lines denote fermions. These densities are obtained from solving the Vlasov equation using the method of [27], assuming CDM halos with the Navarro–Frenk–White density profile [equation (B.8)].

3. Nonlinear structure formation

At late times ($z \lesssim 100$), fluctuations in the mass density field can become larger than unity. Linear perturbation theory breaks down, and structure formation enters a nonlinear phase with the collapse of overdense regions into gravitationally bound objects. In hierarchical CDM cosmologies, nonlinear gravitational collapse begins at small scales, and the nature of the CDM particle determines the size of the first objects. Subsequent mergers of these small systems give rise to larger structures—from the halos of dwarf galaxies to the filaments and the voids. In terms of Fourier decomposition, the transition from the linear to the nonlinear regime in the density field occurs roughly at $k \sim 0.2\ h\ \mathrm{Mpc}^{-1}$ today.

The effect of HDM on nonlinear clustering and its statistics is twofold. Firstly,

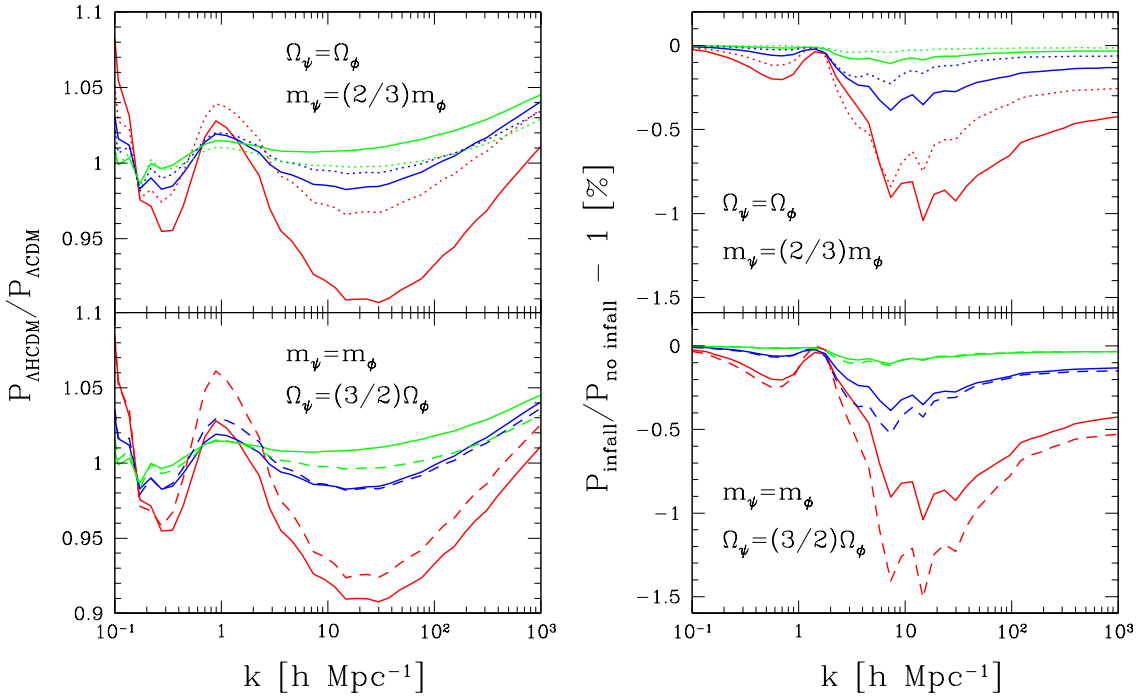

Figure 3. *Left*: Nonlinear power spectra at $z = 0$ for $g_* = 10.75$ and various HDM masses, relative to the standard ΛCDM power spectrum. Solid lines denote bosons of masses (top to bottom) $\{0.3, 0.6, 1.2\}$ eV, dotted lines are for $\{0.2, 0.4, 0.8\}$ eV fermions, while dashed lines represent $\{0.3, 0.6, 1.2\}$ eV fermions. These masses are chosen such that they satisfy either $\Omega_\psi = \Omega_\phi$ or $m_\psi = m_\phi$. Note that all spectra here have been normalised to a fixed value of σ_8. *Right*: Relative contributions from HDM infall for the same HDM scenarios.

free-streaming of HDM in the early (linear) stages of structure formation suppresses density fluctuations on scales below $\lambda_{\rm FS}$. This directly limits the number of small scale structures that can be formed subsequently in the nonlinear phase.

Secondly, at late times, secondary infall of HDM into existing CDM halos becomes possible when the former's mean velocity,

$$\langle v\rangle \simeq f \times 23\ (1+z)\left(\frac{10.75}{g_*}\right)^{1/3}\left(\frac{\rm eV}{m_{\rm HDM}}\right)\ {\rm km\ s^{-1}}, \quad f = \begin{cases} 7 & \text{FD} \\ 6 & \text{BE} \end{cases} \tag{3.1}$$

drops below the velocity dispersion of the astrophysical system concerned. A typical galaxy cluster ($M \sim 10^{14} \to 10^{15}\ M_\odot$) has a velocity dispersion of about 1000 km s^{-1} today; a typical galaxy ($M \sim 10^{12}\ M_\odot$), about 200 km s^{-1}. Thus, for $m_{\rm HDM} \sim 1$ eV, a good fraction of HDM particles can be expected to reside presently in halos across a wide mass range. Figure 2 shows a sample of HDM overdensities expected for a scalar and a Majorana fermion for a range of halo masses. These are obtained from solving the Vlasov equation (A.1), assuming CDM halo density profiles of the Navarro–Frenk–White form [equation (B.8)] [25, 26]. A brief description of this calculation can be found in Appendix A. For more details, see reference [27].

Observe in Figure 2 that at the sub-Mpc scales, bosons cluster considerably more

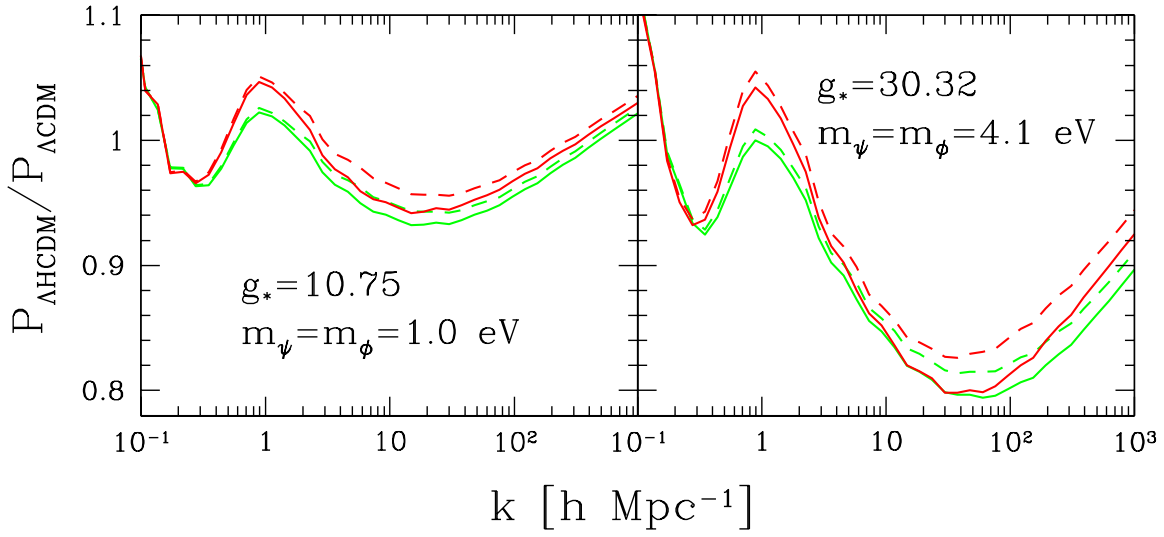

Figure 4. Nonlinear power spectra at $z = 0$ for two different values of g_*, relative to the standard ΛCDM power spectrum. Red (dark) lines denote fermions, while green (light) lines represent bosons. Solid lines show the power spectra with HDM infall, dashed lines show them without.

efficiently than do fermions. This is because, at any given temperature, the unperturbed phase space distribution for bosons is more skewed towards the low momenta, making the particles more susceptible to capture by the CDM halos. Furthermore, the final HDM phase space distribution in a halo is, in general, subject to constraints imposed by Liouville's theorem, and hence must not exceed the maximum of the initial unperturbed distribution function, $f_{\rm final} \lesssim f^{\rm max}_{\rm initial}$ [28]. For fermions with no chemical potential, the maximum $f^{\rm max}_{\rm initial} = 1/2$ occurs at $p = 0$. Using this line of argument, Tremaine and Gunn have famously derived a bound on the maximum possible neutrino density in a halo [29, 30]. Bosons, however, are technically not subject to the same constraint, since no finite maximum exists in their initial phase space distribution. Thus, correspondingly in Figure 2, the overdensity of bosons is seen to be much higher than that of fermions with the same mass.

Note, however, that the Tremaine–Gunn bound is still applicable to bosons in a statistical sense because only a very small fraction of all thermally produced bosons reside in low momentum states [31, 32]. (One notable exception is axion cold dark matter which consists of low mass bosons in a condensate.)

3.1. The nonlinear power spectrum

In Figures 3 to 5, we show predictions for the nonlinear power spectrum at $z = 0$ for a variety of scenarios involving bosonic and fermionic HDM. These spectra are calculated from a phenomenological approach known as the halo model [33, 34, 35, 36], extended to include contributions from HDM infall [37]. While the halo model will not serve for high precision cosmology, it suffices to illustrate the typical scales of the various effects

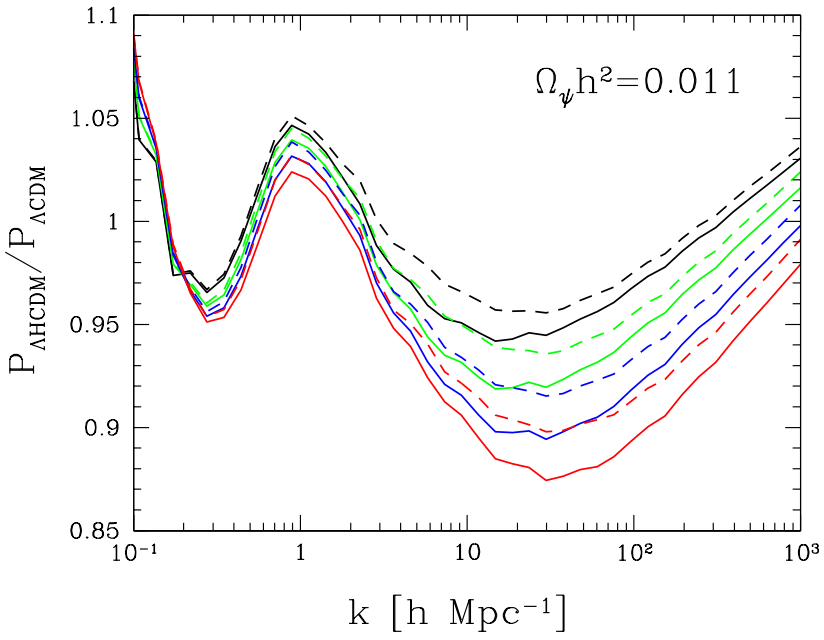

Figure 5. Nonlinear power spectra at $z = 0$ for fermions with various values of g_* and m_ψ but the same $\Omega_\psi h^2 = 0.011$, relative to the standard ΛCDM power spectrum. Solid lines show the power spectra with HDM infall, dashed lines without. From top to bottom: $m_\psi = \{1, 1.41, 2.00, 2.82\}$ eV, corresponding to $g_* = \{10.75, 15.16, 21.5, 30.32\}$.

due to HDM. See Appendix B for more details.

As is evident in the Figures, early HDM free-streaming is generally the dominant influence on the shape of the nonlinear power spectrum. Ignoring contributions from late-time infall, one can see that early free-streaming alone already distinguishes between fermions and bosons, and between cases with different g_*'s at the percent level. Late-time HDM infall causes additional losses of power at $k \gtrsim 1\ h$ Mpc^{-1}, because HDM clustering tends to "smooth out" the overall matter distribution within the individual halo. For the $g_* = 10.75$ cases (Figure 3), losses from infall are typically no more than one percent, and occur at scales corresponding to roughly ten times the *current* free-streaming wavenumber of the particle $k_{\rm FS}$,

$$k_{\rm FS} \simeq f \times 0.11 \sqrt{\frac{\Omega_m}{1+z}} \left(\frac{g_*}{10.75}\right)^{1/3} \left(\frac{m_{\rm HDM}}{\rm eV}\right)\ h\ {\rm Mpc}^{-1}. \tag{3.2}$$

The analysis of [37] also finds a reduction of power due to infall at the $0.1 \rightarrow 1$ % level, albeit at a scale of $k \sim 0.5\ h$ Mpc^{-1}. This discrepancy could be due to the linear method used in their clustering calculations.

Infall increases in importance for cases with $g_* > 10.75$. This is because these particles are colder, and for the same $\Omega_{\rm HDM}$, are heavier; both attributes allow them to cluster more efficiently. Indeed, as shown in Figures 4 and 5, HDM infall in any one scenario can alter the resulting power spectrum to the extent that it mimics another scenario, and is therefore potentially important for high precision cosmology. Examples

of thermal relics with large g_*'s include very light gravitinos ($g_* \sim 100$, corresponding to a decoupling temperature of a few GeV to a few TeV), and thermally produced axions ($10.75 \lesssim g_* \lesssim 80$, corresponding to decoupling during the QCD phase transition).

4. Observational probes

4.1. Weak gravitational lensing

Weak gravitational lensing of distant galaxies by intervening large scale structure provides a unique method to directly map the matter distribution in the universe (e.g., [38]). Perturbations in the gravitational potential along the line of sight induce distortions in the images of distant galaxies. The images may be magnified (convergence) and/or stretched (shear). For weak lensing of a large ensemble of sources and lenses, it can be shown that the convergence and the shear have identical statistical properties. Henceforth, we shall consider the power spectrum of the convergence as representative of the lensing features.

The convergence is essentially an integral over all the deflectors between us and the source galaxies, weighted by the source galaxy distribution. Its power spectrum at multipole ℓ can be related to the matter power spectrum $P(k, z)$ via [38, 39, 40]

$$C_\ell = \frac{9}{16}\, H_0^4\, \Omega_m^2 \int_0^{\chi_h} d\chi \left[\frac{g(\chi)}{a\chi}\right]^2 P\left(\frac{\ell}{\chi}, z\right) , \tag{4.1}$$

in a flat universe. Here, $\chi = \int_0^z dz/H(z)$ is the comoving radial distance, and χ_h is the distance to the horizon. The weak lensing weighting function,

$$g(\chi) = \chi \int_\chi^{\chi_h} d\chi'\; n(\chi')\; \frac{\chi' - \chi}{\chi'} , \tag{4.2}$$

encapsulates information about the source galaxy redshift distribution $n(\chi)$. For our purposes, $n(\chi)$ may be taken to be $n(z) \propto z^\alpha \exp[-(z/z_0)^\beta]$, where the parameters z_0, α and β are estimated from existing deep redshift surveys for the weak lensing survey at hand [41, 42]. The prefactor is determined by the normalisation condition $\int dz\, n(z) = 1$. In the following, we shall take $z_0 = 1$, $\alpha = 2$ and $\beta = 2$, typical of most proposed large scale lensing surveys [42]. With these parameters, the weak lensing weighting function (4.2) peaks at $z \sim 0.4 \to 0.5$.

In any lensing survey, the ability to measure C_ℓ is constrained on large scales by a sample variance due to finite sky coverage, and on small scales by the finite number of available galaxies. Neglecting non-Gaussian corrections, the statistical error in C_ℓ is estimated to be [39, 40]

$$\Delta C_\ell = \sqrt{\frac{2}{(2\ell+1) f_{\rm sky}}} \left(C_\ell + \frac{\gamma_{\rm rms}^2}{n_{\rm gal}}\right) , \tag{4.3}$$

where $f_{\rm sky}$ is the fraction of the sky covered by the survey, $n_{\rm gal}$ is the surface density of galaxies, and $\gamma_{\rm rms}$ is the rms shear per galaxy (from noise and intrinsic ellipticity). These parameters are generally survey dependent. Proposed wide-field surveys such as

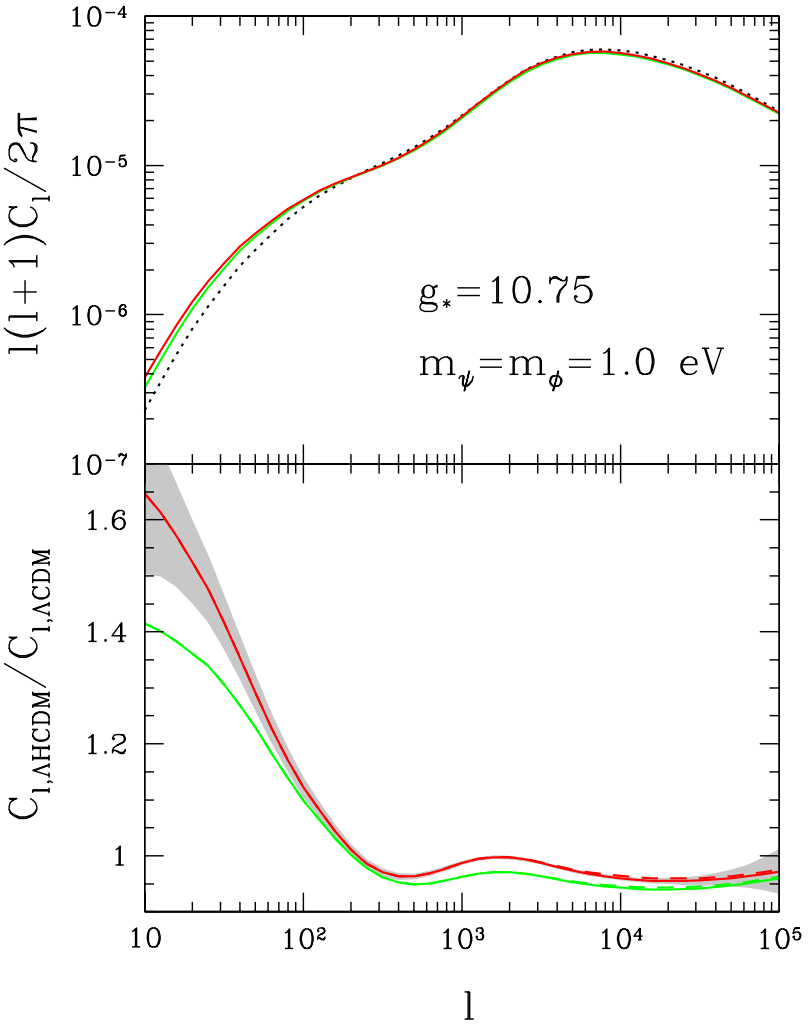

Figure 6. *Top*: Weak lensing convergence power spectra for the models shown in the left panel of Figure 4. The red (dark solid) line denotes fermions, the green (light solid) line represents bosons, while the black (dotted) line corresponds to the standard ΛCDM model. *Bottom*: The same two convergence spectra normalised to the standard ΛCDM convergence spectrum. Solid lines show the spectra with HDM infall, dashed lines show them without. The grey shaded area represents errors expected for a LSST-type survey, smeared over bands of width $\ell/4$. Figure 7 left shows the same plot at $\ell = 10^2 \to 10^5$ for greater clarity.

the Supernova/Acceleration Probe (SNAP) [44] are expected to cover some 1000 deg^2 ($f_{\rm sky} \sim 0.03$) of the sky; the coverage of the more ambitious Large Synoptic Survey Telescope (LSST) [45] will likely be another tenfold. In the ensuing analysis, we shall adopt $\gamma_{\rm rms} = 0.15$, $n_{\rm gal} = 50$ arcmin^{-2}, and $f_{\rm sky} = 0.5$, parameter values corresponding to an optimal LSST-type survey. After smearing over bands of width $\ell/4$, we have approximately

$$\Delta C_l \simeq 0.004 \frac{1000}{\ell} \sqrt{\frac{0.25}{f_{\rm sky}}} \left(C_\ell + \frac{\gamma_{\rm rms}^2}{n_{\rm gal}} \right) \tag{4.4}$$

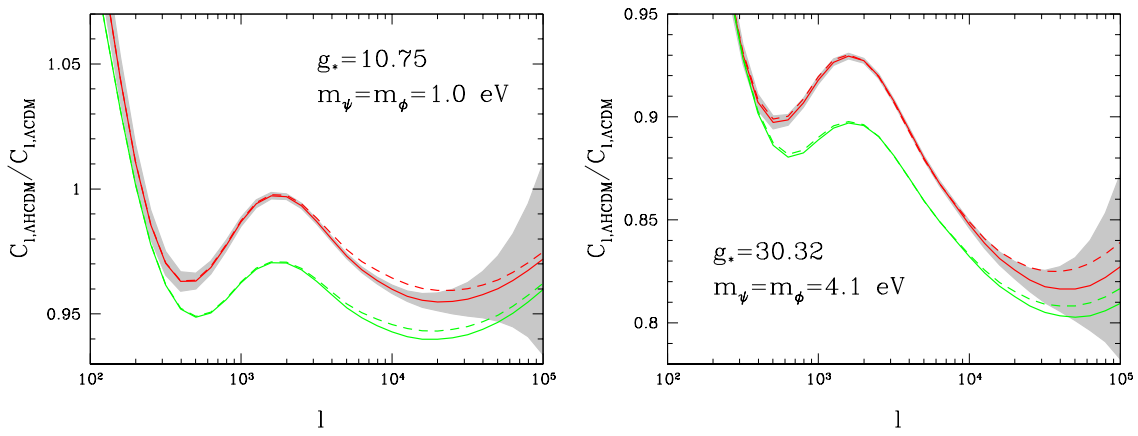

Figure 7. Weak lensing convergence power spectra for the models shown in Figure 4, relative to the standard ΛCDM convergence spectrum. Red (dark) lines denote fermions, while green (light) lines represent bosons. Solid lines show the spectra with HDM infall, dashed lines show them without.

as the effective error [43].

Figures 6 to 9 show the expected weak lensing convergence power spectra for the various HDM scenarios considered in the previous section. The general shapes of the convergence spectra are similar to those of their corresponding matter power spectra shifted according to $k \approx \ell/1000$, and reflect predominantly the early free-streaming behaviours of the different HDM species. Contributions from infall, however, are considerably reduced (by a factor of $2 \rightarrow 3$) relative to the $z = 0$ matter power spectrum. This is because weak lensing is primarily sensitive to the $z \sim 0.4 \rightarrow 0.5$ universe, where the amount of HDM infall is correspondingly lower.

In Figures 7 and 8, we see that the contributions from infall are typically at the sub-percent level at $\ell \sim 10^3 \rightarrow 10^4$. As with the nonlinear power spectrum, the contributions increase with g_* and $m_{\rm HDM}$. However, because the scale at which HDM infall is manifest depends on the *current* free-streaming scale of the HDM particle [cf. equation (3.2)], the signatures of infall are also shifted accordingly to larger values of ℓ, where the statistical errors are larger. The net result is that there may only be a very narrow window in $m_{\rm HDM}$ and g_* in which HDM infall has some observable consequences in weak lensing, even for an optimal LSST-type lensing survey. Judging from Figures 7 and 8, we estimate this window to be $1 \lesssim m_{\rm HDM}/{\rm eV} \lesssim 4$ and $g_* \lesssim 30$.

Nevertheless, fermionic and bosonic HDM can still be distinguished by their early free-streaming behaviours. In Figure 9, we see that this is possible for an LSST-type lensing survey for particles as light as $m_{\rm HDM} \sim 0.2$ eV.

4.2. Strong gravitational lensing

Looking at Figure 2, it is clear that the main difference between fermionic and bosonic HDM is in the central regions of halos. The matter distribution in the central parts

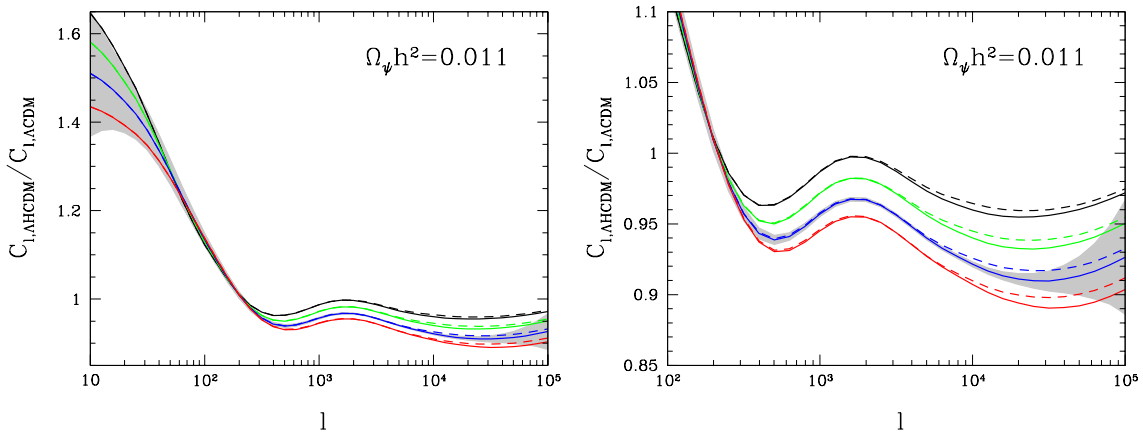

Figure 8. *Left*: Weak lensing convergence power spectra for the $\Omega_\psi h^2 = 0.011$ models shown in Figure 5, relative to the standard ΛCDM convergence spectrum. Solid lines show the spectra with HDM infall, dashed lines without. The masses of the HDM particles are (top to bottom) $\{1, 1.41, 2.00, 2.82\}$ eV, corresponding to $g_* = \{10.75, 15.16, 21.5, 30.32\}$. *Right*: Same as the left panel, but zoomed in on $\ell = 10^2 \to 10^5$.

of dark matter halos can in principle be probed by strong gravitational lensing, either by very precise measurements of a single lensing system [46, 47, 48], or by measuring a very large sample of systems (for instance using a supernova survey [49]). However, even though difference between fermions and bosons is large, the total contribution of HDM in the central part of a halo is only a minute fraction of the total matter density. The ratio $\rho_{\rm HDM}/\rho_{\rm CDM}$ decreases with decreasing r and therefore HDM is most easily probed on scales comparable to, or larger than, the virial radius where weak lensing is most efficient.

5. Conclusions

We have studied the difference between fermionic and bosonic hot dark matter in detail. In the linear regime of structure formation, the most important difference is that for equal contributions to the present energy density, the mass of a scalar species is higher than that of a fermion by a factor 3/2. This in turn means that scalars have a smaller free-streaming length and therefore less suppression of fluctuation power. This effect is most pronounced around the free-streaming scale, where the difference can be of order $30 \to 40$ % in terms of the present day linear power spectrum. At present, the difference is too small to be discerned by available cosmological data (as also discussed in the context of nonthermally distributed neutrinos [50]), but may be visible in the next generation of probes for large scale structure and in proposed wide-field weak gravitational lensing surveys.

In the nonlinear regime, there is a fundamental difference between fermions and bosons arising from the fact that the phase space distribution for fermions is subject to constraints imposed by Liouville's theorem, while for bosons there is no formal upper

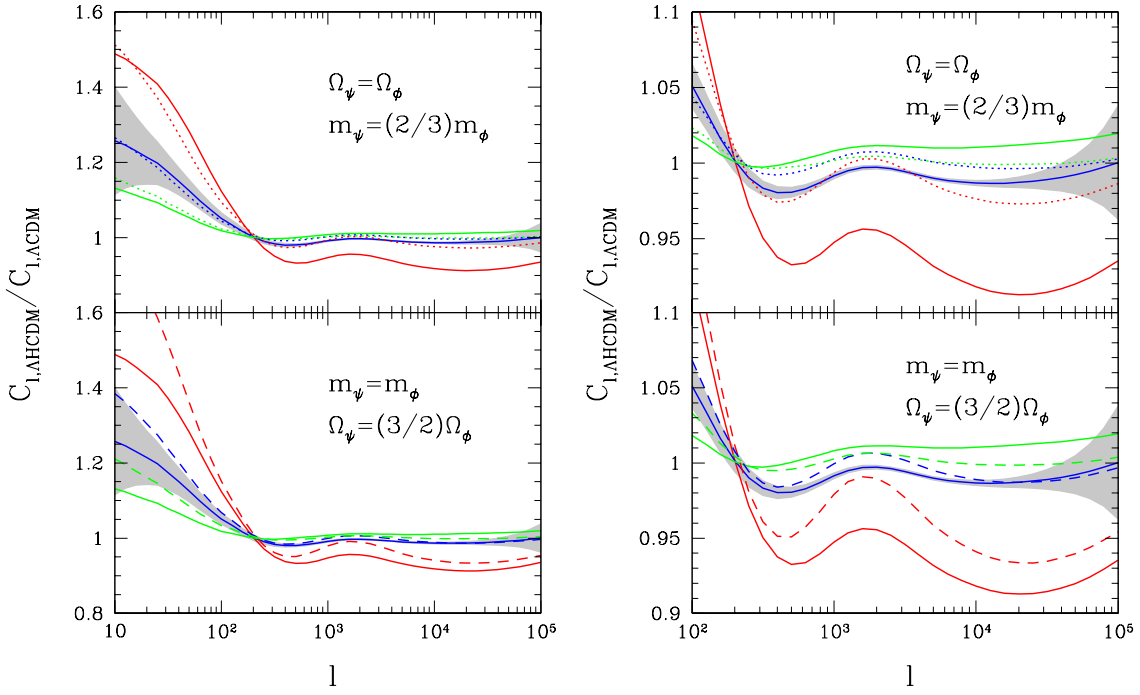

Figure 9. *Left*: Weak lensing convergence power spectra for the $g_* = 10.75$ models shown in Figure 3, relative to the standard ΛCDM convergence spectrum. Solid lines denote bosons of masses (top to bottom) $\{0.3, 0.6, 1.2\}$ eV, dotted lines are for $\{0.2, 0.4, 0.8\}$ eV fermions, while dashed lines correspond to $\{0.3, 0.6, 1.2\}$ eV fermions. *Right*: Same as the left panel, but zoomed in on $\ell = 10^2 \rightarrow 10^5$.

bound. This difference has a direct impact on the particles' clustering properties. In order to probe this phenomenon, we have studied late-time hot dark matter infall into cold dark matter halos, and find that, in the central part of a halo, the difference between the fermionic and bosonic overdensities can be more than a factor five. While this difference appears large, it is not likely to be observable by direct means (e.g., by strong gravitational lensing) simply because the density of hot dark matter is so small in the central regions of halos.

Instead, we have considered the implications of hot dark matter for the nonlinear power spectrum, $k \gtrsim 0.2\ h\ \mathrm{Mpc}^{-1}$. These are the scales at which future weak lensing surveys have the most statistical power. Using a halo model approach, we find that the early free-streaming behaviour of the hot dark matter species remains the dominant influence on the shape of the resulting nonlinear power spectrum. In some cases, notably thermal relics with $g_* \gtrsim 10.75$, hot dark matter infall can contribute an additional loss of power at the percent level at $z = 0$, depending on their masses and quantum statistics. This suggests that infall can potentially play a decisive role in high precision cosmology. However, because both the amount of hot dark matter infall and the scale at which it is manifest depend crucially on the values of g_* and m_{HDM}, signatures of infall may end up unobservable in the weak lensing convergence spectrum, even with a Large Synoptic Survey Telescope-type lensing survey, unless $g_* \lesssim 30$ and $1 \lesssim m_{\mathrm{HDM}}/\mathrm{eV} \lesssim 4$.

The bottom line is that the difference in the hot dark matter contribution arising from quantum statistics is a very interesting example of statistical mechanics, but that it may prove to be very difficult to observe. On the other hand, imprints on the matter power spectrum from different early free-streaming behaviours extend to both the linear and the nonlinear scales. These could well be observable with future experiments if the mass of the hot dark matter species is sufficiently large (say, $m_{\rm HDM} \gtrsim 0.2$ eV).

Appendix A. Hot dark matter clustering

The problem of late time HDM clustering in the presence of a CDM halo can be treated quantitatively with the nonrelativistic Vlasov equation (e.g., [51]),

$$\frac{\partial f_i}{\partial \tau} + \frac{\boldsymbol{p}}{a m_i} \cdot \frac{\partial f_i}{\partial \boldsymbol{x}} - a m_i \nabla \phi \cdot \frac{\partial f_i}{\partial \boldsymbol{p}} = 0, \qquad i = \text{CDM, HDM}, \tag{A.1}$$

which tracks the evolution of the phase space densities $f_i(\boldsymbol{x}, \boldsymbol{p}, \tau)$ under the influence of the peculiar gravitational potential $\phi(\boldsymbol{x}, \tau)$ as functions of comoving position $\boldsymbol{x}$, momentum $\boldsymbol{p}$, and conformal time τ. In turn, $\phi(\boldsymbol{x}, \tau)$ is related to the local density fluctuations $\delta_i(\boldsymbol{x}, \tau)$ via the Poisson equation,

$$\nabla^2 \phi = \frac{4\pi G}{a} \sum_i \bar{\rho}_i \, \delta_i(\boldsymbol{x}, \tau), \tag{A.2}$$

where

$$\delta_i(\boldsymbol{x}, \tau) \equiv \frac{\rho_i(\boldsymbol{x}, \tau)}{\bar{\rho}_i} - 1, \qquad \rho_i(\boldsymbol{x}, \tau) = m_i \int d^3p \; f_i(\boldsymbol{x}, \boldsymbol{p}, \tau), \tag{A.3}$$

and $\bar{\rho}_i$ denotes the ith comoving mean density.

A number of methods are available for solving equations (A.1) and (A.2)—from numerical simulations to semi-analytical approaches under a variety of approximation schemes—with varying degrees of accuracy. In this work, we use a restricted N-single-body method introduced in [27]. Here, test particles sampled from the initial HDM phase space distribution are allowed to evolve, one at a time, in an external potential $\phi(\boldsymbol{x}, \tau)$ due to the CDM halo alone. Gravitational interactions between the HDM particles themselves are explicitly ignored, which is well justified considering current cosmological constraints on the HDM mass fraction today ($\Omega_{\rm HDM}/\Omega_m \lesssim 0.1$). Compared with other solution methods, our N-single-body approach is computationally inexpensive relative to full-scale N-body simulations, and is yet able to reproduce essential nonlinear effects not captured by simpler, linear methods (e.g., [52]). See reference [27] for more details.

Appendix B. The halo model

The halo model supposes that all matter in the universe is partitioned into distinct units, the halos. This assumption allows one to study the universal matter distribution in two steps: the distribution of matter within each halo, and the spatial distribution

of the halos themselves. In its simplest application, the halo model proposes that the matter power spectrum $P(k,z)$ be composed of two distinct terms (e.g., [36]),

$$P(k,z) = P^{1-\mathrm{halo}}(k,z) + P^{2-\mathrm{halo}}(k,z), \tag{B.1}$$

where

$$P^{1-\mathrm{halo}}(k,z) = \int dM\ n(M,z) \left(\frac{M}{\bar{\rho}_{\mathrm{halo}}}\right)^2 |u(k|M)|^2,$$
$$P^{2-\mathrm{halo}}(k,z) = P^{\mathrm{lin}}(k,z) \left[\int dM\ n(M,z)\ b(M) \left(\frac{M}{\bar{\rho}_{\mathrm{halo}}}\right) u(k|M)\right]^2, \tag{B.2}$$

describe, respectively, the correlations between two points drawn from the same halo ("1-halo") and from two different halos ("2-halo"). The former dominates on small scales (i.e., large k's), while the latter rises to prominence on large scales (i.e., small k's) and approaches the power spectrum calculated from linear perturbation theory $P^{\mathrm{lin}}(k,z)$ as $k \to 0$. The average (comoving) matter density $\bar{\rho}_{\mathrm{halo}}$ counts all matter clustered in halos. For a basic ΛCDM set-up, $\bar{\rho}_{\mathrm{halo}}$ is well approximated by $\bar{\rho}_{\mathrm{halo}} \simeq \bar{\rho}_m \equiv \Omega_m \rho_{\mathrm{crit}}$, where ρ_{crit} is the present critical density.

Three pieces of information are required to complete the model.

(i) The mass function $n(M,z)$ specifies the comoving number density of halos of virial mass M at redshift z. Following from the Press–Schechter theory [53], this is usually written as

$$n(M,z)\ dM = \frac{\bar{\rho}_{\mathrm{halo}}}{M} f(\nu)\ d\nu, \tag{B.3}$$

where $f(\nu)$ is a universal function of the peak height $\nu = \delta_{\mathrm{sc}}^2/\sigma_{\mathrm{lin}}^2(M,z)$. Here, $\delta_{\mathrm{sc}} = 1.68$ is the linear overdensity at the epoch of spherical collapse, and

$$\sigma_{\mathrm{lin}}^2(M,z) \equiv \int \frac{d^3k}{(2\pi)^3} P^{\mathrm{lin}}(k,z) |W(kR)|^2 \tag{B.4}$$

is the rms of the linear fluctuations filtered with a tophat window function $W(x) = 3/x^3(\sin x - x\cos x)$ on a scale of $R = (3M/4\pi\bar{\rho}_m)^{1/3}$. In this way, every halo mass M is associated with a unique value of ν, with large ν's corresponding large halo masses and so forth. A number of variants for the function $f(\nu)$ exists in the literature. Here, we adopt the version proposed by Sheth and Tormen [54],

$$\nu f(\nu) = A\left(1 + (q\nu)^{-p}\right)\sqrt{\frac{q\nu}{2\pi}}\exp(-q\nu/2), \tag{B.5}$$

with $p = 0.3$ and $q = 0.707$, based on fits to N-body simulations. The constant A is determined by mass conservation, i.e., $\int dM\ n(M,z)\ M = \bar{\rho}_{\mathrm{halo}}$, or, equivalently, $\int d\nu\ f(\nu) = 1$.

(ii) The linear bias $b(\nu)$ parameterises the clustering strength of halos relative to the underlying dark matter, and obeys $\int d\nu\ f(\nu)\ b(\nu) = 1$ by construction. For the Sheth–Tormen mass function (B.5), the associated bias is [54]

$$b(\nu) = 1 + \frac{q\nu - 1}{\delta_{\mathrm{sc}}} + \frac{2p/\delta_{\mathrm{sc}}}{1 + (q\nu)^p}. \tag{B.6}$$

(iii) The function $u(k|M)$ is the Fourier transform at wavenumber k of the matter distribution $\rho(r|M)$ within a halo of mass M, normalised to the halo mass. For spherically symmetric density profiles $\rho(r|M)$ truncated at the virial radius $r_{\rm vir}$ (to be defined below), this is given by

$$u(k|M) \equiv \frac{\tilde{\rho}(k|M)}{M} = \int_0^{r_{\rm vir}} dr\ 4\pi r^2\ \frac{\sin kr}{kr} \frac{\rho(r|M)}{M}. \tag{B.7}$$

In the simplest case where only CDM and baryons cluster, a natural choice for $\rho(r|M)$ is the Navarro–Frenk–White (NFW) profile [25, 26],

$$\rho(r|M) = \frac{\rho_s}{(r/r_s)(1+r/r_s)^2}\,, \tag{B.8}$$

which has proven to provide a very good description of the density run around virialised halos in high resolution N-body simulations in a variety of CDM cosmologies. Here, r is the radial distance from the halo centre. The parameters r_s and ρ_s are determined by the halo's virial mass M and a dimensionless concentration $c \equiv r_{\rm vir}/r_s$ via

$$\rho_s = \frac{\delta_{\rm TH}}{3} \frac{c^3}{\ln(1+c) - c/(1+c)}, \tag{B.9}$$

$$r_s = \frac{r_{\rm vir}}{c} = \frac{1}{c}\left(\frac{3}{4\pi\delta_{\rm TH}} \frac{M}{\bar{\rho}_m}\right)^{1/3}, \tag{B.10}$$

where $\delta_{\rm TH}$ is the virial overdensity predicted by the spherical top-hat collapse model [55],

$$\delta_{\rm TH} \simeq \frac{18\pi^2 + 82y - 39y^2}{\Omega(z)},$$
$$y = \Omega(z) - 1, \qquad \Omega(z) = \frac{\Omega_m}{\Omega_m + \Omega_\Lambda a^3}. \tag{B.11}$$

In addition, a tight correlation between c and M has been observed in the analysis of [56],

$$c(z) \simeq \frac{9}{1+z}\left(\frac{M}{M^*}\right)^{-0.13}, \tag{B.12}$$

where $M^* = M(\nu = 1)$ denotes the $P^{\rm lin}$-dependent nonlinear mass.

Several modifications to the halo model have been discussed in the literature, to account for, e.g., the effects of baryons [43, 57], neutrino infall [37], etc.. To include the effects of HDM infall, we follow the prescription of [37] by defining

$$M \equiv M_{\rm CDM+b} + M_{\rm HDM}, \tag{B.13}$$

$$u(k|M) \equiv \frac{\tilde{\rho}_{\rm HDM}(k|M) + \tilde{\rho}_{\rm CDM+b}(k|M)}{M_{\rm CDM+b} + M_{\rm HDM}}, \tag{B.14}$$

where M_i and $\tilde{\rho}_i(k|M)$ denote, respectively, contributions from the i type particles to the total halo mass and Fourier transform of the density profile. Furthermore, the quantity

$\bar{\rho}_{\rm halo}$ should account also for HDM residing in halos, i.e., $\bar{\rho}_{\rm halo} = \bar{\rho}_{\rm CDM} + \bar{\rho}_b + \bar{\rho}_{\rm HDM,halo} \simeq (\Omega_{\rm CDM} + \Omega_b)\rho_{\rm crit} + \bar{\rho}_{\rm HDM,halo}$, where

$$\bar{\rho}_{\rm HDM,halo} = \bar{\rho}_{\rm halo} \int d\nu f(\nu) \frac{M_{\rm HDM}}{M}. \tag{B.15}$$

Note that, in general, $\rho_{\rm HDM,halo} \ll \Omega_{\rm HDM}\rho_{\rm crit}$, since the HDM's significant thermal energy prevents a large fraction of particles from participating in the infall.

References

[1] A. G. Riess *et al.* [Supernova Search Team Collaboration], Astron. J. **116** (1998) 1009 [arXiv:astro-ph/9805201].
[2] S. Perlmutter *et al.* [Supernova Cosmology Project Collaboration], Astrophys. J. **517** (1999) 565 [arXiv:astro-ph/9812133].
[3] D. N. Spergel *et al.* [WMAP Collaboration], Astrophys. J. Suppl. **148** (2003) 175 [arXiv:astro-ph/0302209].
[4] M. Tegmark *et al.* [SDSS Collaboration], Phys. Rev. D **69** (2004) 103501 [arXiv:astro-ph/0310723].
[5] S. S. Gershtein and Y. B. Zeldovich, JETP Lett. **4** (1966) 120 [Pisma Zh. Eksp. Teor. Fiz. **4** (1966) 174].
[6] R. Cowsik and J. McClelland, Phys. Rev. Lett. **29** (1972) 669.
[7] E. W. Kolb and M. S. Turner, *The Early Universe*, Addison–Wesley (1990).
[8] M. Viel, J. Lesgourgues, M. G. Haehnelt, S. Matarrese and A. Riotto, Phys. Rev. D **71** (2005) 063534 [arXiv:astro-ph/0501562].
[9] W. Hu, D. J. Eisenstein and M. Tegmark, Phys. Rev. Lett. **80** (1998) 5255 [arXiv:astro-ph/9712057].
[10] S. Hannestad, JCAP **0305** (2003) 004 [arXiv:astro-ph/0303076].
[11] O. Elgaroy and O. Lahav, New J. Phys. **7** (2005) 61 [arXiv:hep-ph/0412075].
[12] V. Barger, D. Marfatia and A. Tregre, Phys. Lett. B **595** (2004) 55 [arXiv:hep-ph/0312065].
[13] P. Crotty, J. Lesgourgues and S. Pastor, Phys. Rev. D **69** (2004) 123007 [arXiv:hep-ph/0402049].
[14] U. Seljak *et al.*, arXiv:astro-ph/0407372.
[15] G. L. Fogli, E. Lisi, A. Marrone, A. Melchiorri, A. Palazzo, P. Serra and J. Silk, Phys. Rev. D **70** (2004) 113003 [arXiv:hep-ph/0408045].
[16] M. Tegmark, arXiv:hep-ph/0503257.
[17] S. Hannestad, arXiv:astro-ph/0505551.
[18] S. Hannestad and G. Raffelt, JCAP **0404** (2004) 008 [arXiv:hep-ph/0312154].
[19] T. Moroi and H. Murayama, Phys. Lett. B **440** (1998) 69 [arXiv:hep-ph/9804291].
[20] S. Hannestad, A. Mirizzi and G. Raffelt, arXiv:hep-ph/0504059.
[21] M. Ibe, K. Tobe and T. Yanagida, Phys. Lett. B **615** (2005) 120 [arXiv:hep-ph/0503098].
[22] A. Brandenburg and F. D. Steffen, JCAP **0408** (2004) 008 [arXiv:hep-ph/0405158].
[23] A. D. Dolgov and A. Y. Smirnov, arXiv:hep-ph/0501066.
[24] A. D. Dolgov, S. H. Hansen and A. Y. Smirnov, arXiv:astro-ph/0503612.
[25] J. F. Navarro, C. S. Frenk and S. D. M. White, Astrophys. J. **462** (1996) 563 [arXiv:astro-ph/9508025];
[26] J. F. Navarro, C. S. Frenk and S. D. M. White, Astrophys. J. **490** (1997) 493.
[27] A. Ringwald and Y. Y. Y. Wong, JCAP **0412** (2004) 005 [arXiv:hep-ph/0408241].
[28] J. Binney and S. Tremaine, *Galactic Dynamics*, Princeton University Press (1987).
[29] S. Tremaine and J. E. Gunn, Phys. Rev. Lett. **42** (1979) 407.
[30] A. Kull, R. A. Treumann and H. Böhringer, Astrophys. J. **466** (1996) L1 [arXiv:astro-ph/9606057].
[31] J. Madsen, Phys. Rev. Lett. **64** (1990) 2744.
[32] J. Madsen, Phys. Rev. D **44** (1991) 999.
[33] U. Seljak, Mon. Not. Roy. Astron. Soc. **318** (2000) 203 [arXiv:astro-ph/0001493].

[34] J. A. Peacock and R. E. Smith, Mon. Not. Roy. Astron. Soc. **318** (2000) 1144 [arXiv:astro-ph/0005010].
[35] C. P. Ma and J. N. Fry, Astrophys. J. 543 (2000) 503, [arXiv:astro-ph/0003343].
[36] A. Cooray and R. Sheth, Phys. Rept. **372** (2002) 1 [arXiv:astro-ph/0206508].
[37] K. Abazajian, E. R. Switzer, S. Dodelson, K. Heitmann and S. Habib, Phys. Rev. D **71** (2005) 043507 [arXiv:astro-ph/0411552].
[38] M. Bartelmann and P. Schneider, Phys. Rept. **340** (2001) 291 [arXiv:astro-ph/9912508].
[39] N. Kaiser, Astrophys. J. **388** (1992) 272.
[40] N. Kaiser, Astrophys. J. **498** (1998) 26 [arXiv:astro-ph/9610120].
[41] R. Massey *et al.*, Astron. J. **127** (2004) 3089 [arXiv:astro-ph/0304418].
[42] A. Refregier *et al.*, Astron. J. **127** (2004) 3102 [arXiv:astro-ph/0304419].
[43] H. Zhan and L. Knox, Astrophys. J. **616** (2004) L75 [arXiv:astro-ph/0409198].
[44] http://snap.lbl.gov
[45] http://www.lsst.org
[46] A. H. Maller, L. Simard, P. Guhathakurta, J. Hjorth, A. O. Jaunsen, R. A. Flores and J. R. Primack, Gravitational Lensing," Astrophys. J. **533** (2000) 194 [arXiv:astro-ph/9910207].
[47] C. M. Trott and R. L. Webster, Mon. Not. Roy. Astron. Soc. **334** (2002) 621 [arXiv:astro-ph/0203196].
[48] C. M. Trott and R. L. Webster, arXiv:astro-ph/0310530.
[49] E. Mortsell, H. Dahle and S. Hannestad, Astrophys. J. **619** (2005) 733 [arXiv:astro-ph/0406343].
[50] A. Cuoco, J. Lesgourgues, G. Mangano and S. Pastor, Phys. Rev. D **71** (2005) 123501 [arXiv:astro-ph/0502465].
[51] E. Bertschinger, in *Les Houches Cosmology 1993*, pp. 273-348, arXiv:astro-ph/9503125.
[52] S. Singh and C. P. Ma, Phys. Rev. D **67** (2003) 023506 [arXiv:astro-ph/0208419].
[53] W. H. Press and P. Schechter, Astrophys. J. **187** (1974) 425.
[54] R. K. Sheth and G. Tormen, Mon. Not. Roy. Astron. Soc. **308** (1999) 119 [arXiv:astro-ph/9901122].
[55] G. L. Bryan and M. L. Norman, Astrophys. J. **495** (1998) 80 [arXiv:astro-ph/9710107].
[56] J. S. Bullock *et al.*, Mon. Not. Roy. Astron. Soc. **321** (2001) 559 [arXiv:astro-ph/9908159].
[57] M. White, Astropart. Phys. **22** (2004) 211 [arXiv:astro-ph/0405593].